Chinese Chemical Letters 36 (2025) 110040

Contents lists available at ScienceDirect

Chinese Chemical Letters

journal homepage: www.elsevier.com/locate/cclet

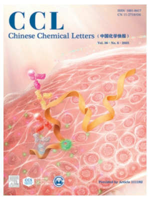

Enabling the Nb/Ti co-doping strategy for improving structure stability and rate capability of Ni-rich cathode

Mingzhu Jiang, Panqing Wang, Qiheng Chen, Yue Zhang, Qi Wu, Lei Tan, Tianxiang Ning, Lingjun Li*, Kangyu Zou*

School of Materials Science and Engineering, Changsha University of Science and Technology, Changsha 410114, China

ARTICLE INFO

Article history:
Received 11 March 2024
Revised 10 May 2024
Accepted 22 May 2024
Available online 23 May 2024

Keywords:
Ni-rich cathode
Dual-element doping
Cationic mixing
Cycling stability
Li-ion batteries

ABSTRACT

High-capacity Ni-rich layered cathodes $LiNi_xCo_yMn_{1-x-y}O_2$ (NCM) have been widely recognized as highly promising candidates for lithium-ion batteries (LIBs). However, NCM cathodes are suffered from sluggish Li-ion kinetics and fast capacity decay. Herein, the Nb/Ti co-doping strategy has been proposed by formation energy analysis to enhance the mechanical and chemical integrities of NCM cathode. Nb/Ti co-doping facilitates Li-ion transport of NCM cathode for boosting the rate ability. Furthermore, the structure stability is prominently improved for the stronger Nb–O and Ti–O bonds, resulting from the suppressed sharp contraction of c axis, inhibited microcracks formation, and alleviated electrolyte corrosion. Inspired by the synergistic effect of Nb/Ti co-doping, the modified NCM exhibits superior comprehensive electrochemical performances. The Nb/Ti co-doping NCM exhibits an increased discharge capacity of 144.3 mAh/g at 10 C and an outstanding capacity retention remained 92.7% after 300 cycles at 1 C. This work offers a promising approach to developing high-performance cathode materials.

The ever-growing demand for high energy and power density for secondary lithium-ion batteries (LIBs) presents a challenge to manufacture cathode materials that possess both high reversible capacity and prolonged cycle life. Layered Ni-rich oxide cathodes ($LiNi_xCo_yMn_{1-x-y}O_2$, $x \geq 0.8$) have garnered extensive interest in both academia and industry, due to their exceptional specific capacity and cost-effectiveness [1-5]. Nonetheless, the commercial application of Ni-rich cathode is still restricted with sluggish Li-ion diffusion and fast capacity decay [6-8]. During the material synthesis process, due to the defect thermodynamics, Ni^{2+} at the 3b site tends to occupy Li^+ at the 3a site, resulting in Li^+/Ni^{2+} mixing, which leads to impeded diffusion of lithium ions and affects the rate performance [9-12]. In addition, Ni-rich cathodes suffer from intergranular cracking, which stemmed from the inhomogeneous strain caused by the dramatic cell shrinkage during the H2-H3 phase transformation [13-15]. Furthermore, corrosive electrolyte penetrates the particle along intergranular cracks, exacerbating hazardous side reactions and generating an electrochemically inactive salt rock phase (Ni–O) [16-21]. The combination of these issues drives rapid capacity degradation and hinders the commercialization of Ni-rich cathodes.

Among diverse modification strategies, elemental doping has been proven to be the most promising for enhancing electrochemical performance by regulating cationic mixing, limiting H2-H3 phase transition, and relieving oxygen evolution [22-24]. It is reported that addictive ions like W^{6+} [25], Nb^{5+} [26], Ta^{5+} [27], Ti^{4+} [28], Al^{3+} [29], Mg^{2+} [30], *etc.* are able to improve the structural stability. For example, Li *et al.* have reported that a super-dispersed Nb doping $LiNi_{0.9}Co_{0.1}MnO_2$ cathode for co-precipitation synthesis addresses the issues of capacity decay and thermal stability [31]. Ti^{4+} doping has been proven to be expected to enhance rate performance owing to improved electronic conductivity and decreased Li^+/Ni^{2+} cationic mixing degree [32,33]. However, a single-element modification strategy can partially mitigate cathode materials failure in specific aspects, whereas the synergistic effect of multi-element doping is anticipated to further comprehend the electrochemical performance [34-36]. At present, the theoretical guidance for the implementation of the multi-element doping strategy in the NCM cathode field is inadequate.

In this work, a co-doping modification strategy has been proposed, utilizing density functional theory (DFT) to calculate the formation energies by introducing Nb and Ti. Nb/Ti co-doping enhances the structure stability for NCM cathode material due to stronger metal-O bonds, which leads to the improvement of electrochemical reversibility and the reduction of polarization. Ti doping effectively suppresses the degree of Li^+/Ni^{2+} mixing,

---

* Corresponding authors.
E-mail addresses: lingjun.li@csust.edu.cn (L. Li), ky-zou@csust.edu.cn (K. Zou).

https://doi.org/10.1016/j.cclet.2024.110040
1001-8417/

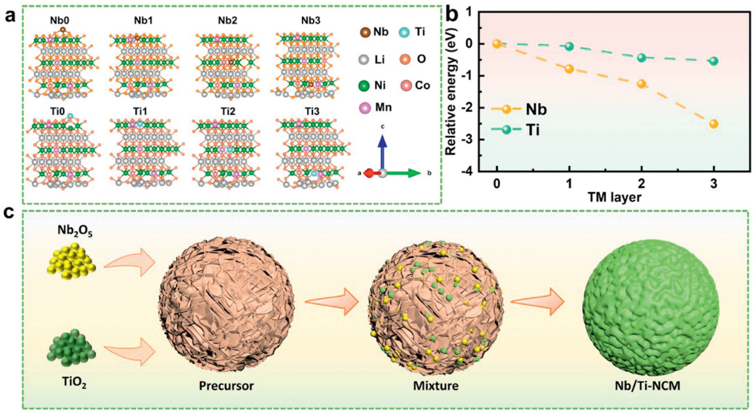

Fig. 1. Theoretical calculations of Nb and Ti modification. The corresponding (a) structures and (b) relative formation energies by introducing Nb and Ti atoms to different Ni layers. (c) Schematic illustration of the synthesis route of the Nb/Ti-NCM cathode.

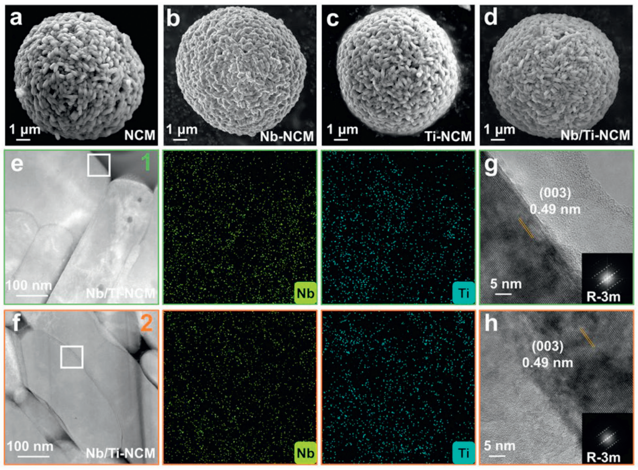

Fig. 2. SEM images of (a) NCM, (b) Nb-NCM, (c) Ti-NCM, (d) Nb/Ti-NCM. TEM-EDS elemental maps of Nb and Ti for (e) region 1 and (f) region 2 of Nb/Ti-NCM cathode. (g, h) HRTEM images of the white squares with FFT patterns of Nb/Ti-NCM cathode.

thereby rate performance is facilitated by improved diffusion of Li^+. The synergistic effect of the Nb/Ti co-doping significantly mitigates the evolution of lattice oxygen, relives lattice distortion during a deeply delithiated state, and limits the formation and propagation for microcracks, while simultaneously decreasing the side reaction with electrolyte. Consequently, the Nb/Ti-NCM cathode demonstrates superior comprehensive electrochemical performances. Nb/Ti-NCM shows splendid rate capability at large current destiny (the rate capacity of 144.3 mAh/g at 10 C), and excellent cycling durability (capacity retention of 92.7% undergoing 300 cycles of 1 C).

To better comprehend the modification mechanism, DFT calculation was employed to evaluate the formation energy for Nb and Ti elements doped into the NCM matrix (Figs. 1a and b). The NCM model was constructed based on $LiNiO_2$ structure, in which a certain proportion of Co, and Mn atoms was introduced. The relative formation energy refers to the energy difference between a single atom of Nb (or Ti) introduced into the *i*th ($i = 1, 2, 3$) of Ni layer within the NCM structure and on the surface. It is noteworthy that the energy of introducing Nb and Ti atoms is consistently lower than the energy compared to their surface energy, indicating that both Nb and Ti elements thermodynamically favor diffusing into the bulk phase. Furthermore, the relative formation energies of Nb and Ti elements are gradually decreased with the increasing doping depth, suggesting a tendency for uniform incorporation within the NCM matrix. Hence, it is expected that a modified NCM cathode with Nb/Ti co-doping can be prepared by simple and low-cost solid-phase calcination (Fig. 1c). The chemical compositions of all samples have been verified by ICP tests (Table S1 in Supporting information).

To investigate the different modification effects of single and double doping with Nb and Ti, the NCM, Nb-NCM, and Ti-NCM samples were synthesized. The particle morphologies of four cathode materials are shown in Figs. 2a–d. There is virtually no difference in morphologies among four samples that display a spherical secondary particle with smooth surfaces and approximately 10 μm in diameter. To further verify the distribution of Nb/Ti elements in NCM cathode, the cross-sections of the outer and inner regions have been applied transmission electron microscopy coupled with energy-dispersive X-ray spectroscopy (TEM-EDS) (Fig. S2 in Supporting information). As presented in Figs. 2e and f and Fig. S3 (Supporting information), the elements Nb, Ti, Ni, Co, and Mn are evenly distributed in all regions. It is indicated that Nb and Ti are homogeneously doped into the bulk phase structure, which aligns well with the results of the DFT calculation. In the high-resolution TEM (HRTEM) images, clear lattice stripes are observed and analysis from fast Fourier transformation (FFT) reveals that the exposed (003) crystallographic plane belongs to the R-3m space group and has a lattice spacing measuring 0.49 nm (Figs. 2g and h). This result confirms that Nb/Ti-NCM remains well crystalline layered structure. Besides, the TEM image of NCM cathode has been shown in Fig. S4 (Supporting information). The (003) plane lattice spacings of NCM is 0.47 nm. Consequently, the co-doping of Nb and Ti effectively broadens the diffusion pathway for lithium ions. XRD patterns for samples are indexed to $LiNiO_2$ crystalline (PDF #74-0919) with the hexagonal α-$NaFeO_2$ and reflection peaks of impurities are undetected (Fig. S5 in Supporting information). To further obtain the value of Li^+/Ni^{2+} mixing and lattice parameters, the XRD Rietveld refinement pattern and intensity ratios of $I_{(003)}/I_{(104)}$ have been illustrated in Figs. 3a and b. The corresponding results have been demonstrated in Fig. 3c and Tables S2–S6 (Supporting information). Notably, the value of Li^+/Ni^{2+} mixing decreases and the unit cell parameters of *a*, *c*, and V expand slightly after Nb or Ti doping, which is basically caused by larger radii of Nb^{5+} (0.69 Å) and Ti^{4+} (0.64 Å) compared with Ni^{3+} (0.56 Å) [37,38]. Remarkably, Ti-NCM shows the lowest cationic mixing degree, indicating that Ti doping should enhance Li-ion migration kinetics [39,40]. To study the different elements and valence compositions, X-ray photoelectron spectroscopy (XPS) characterization was operated at pristine NCM and Nb/Ti-NCM. As revealed in

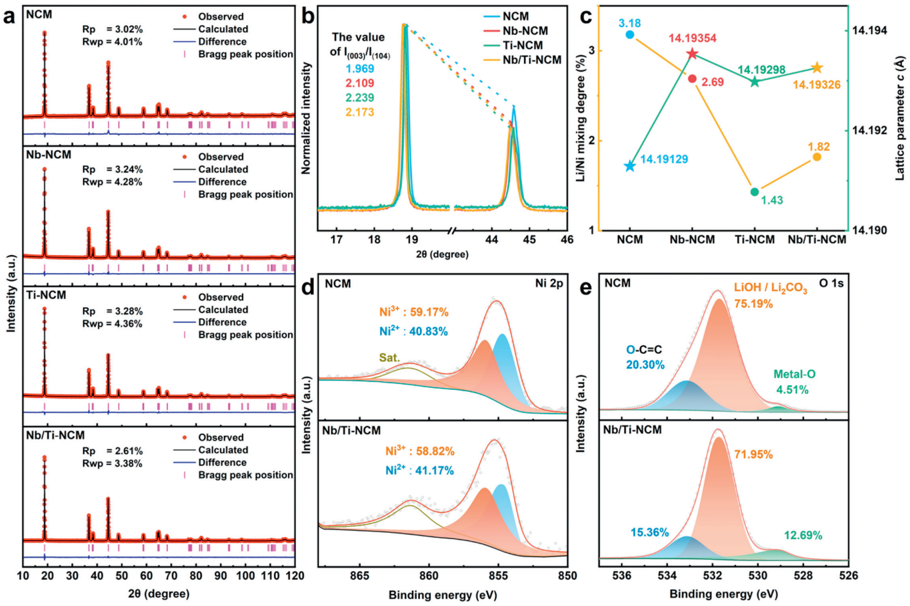

Fig. 3. (a) XRD Rietveld refinements, (b) intensity ratios of (003)/(104) XRD peaks, and (c) Li^+/Ni^{2+} mixing degree and lattice parameter *c* for NCM, Nb-NCM, Ti-NCM, and Nb/Ti-NCM. XPS spectra of (d) Ni 2p, (e) O 1s for NCM and Nb/Ti-NCM.

Fig. 3d, the signal of Ni 2p spectra located at 855.3 eV could be divided into Ni^{3+} and Ni^{2+} cations, respectively [41]. The Ni^{3+}:Ni^{2+} ratios of NCM and Nb/Ti-NCM are 59.17%:40.83% and 58.82%:41.17%, respectively. The Ni^{2+} content on the surface of Nb/Ti-NCM is slightly higher than that of NCM, probably owing to charge compensation. Interestingly, although the Ni^{2+} content is slightly increased, the Li^+/Ni^{2+} mixing is suppressed, which may be due to Nb–O and Ti–O having stronger binding energies, which inhibit the migration of Ni towards the Li sites during synthesis [42,43]. Remarkably, the O 1s spectra for both samples display distinct three peaks at 533.1, 531.8, and 529.1 eV, which matched to species of O–C=O, LiOH/Li_2CO_3, and metal-O, respectively (Fig. 3e). It can be seen that Nb/Ti-NCM with lower O–C=O and LiOH/Li_2CO_3 and higher lattice oxygen content. Besides, the higher content of O–C=O and LiOH/Li_2CO_3 observed in O 1s spectra implicates more surface impurities, which could exacerbate the hazardous side reactions on the surface [44]. Significant Nb 3d and Ti 2p signal peaks are observed in Nb/Ti-NCM, whereas they are absent in NCM, again suggesting that the evolution of the surface chemistry compositions of the material is influenced by Nb/Ti co-doping (Fig. S6 in Supporting information).

To verify the merits of the Nb/Ti co-doping strategy, the electrochemical characteristics of all cathode materials by different Nb/Ti doping ratios were recorded with coin-type half-cells (Fig. S7 in Supporting information). The electrochemical performances of NCM cathode can be effectively improved by introducing the Nb and Ti elements. Notably, the Nb/Ti-NCM delivers the comprehensively boosted electrochemical performances. In detail, the profiles for initial charge/discharge are displayed in Fig. 4a. The initial coulombic efficiency (ICE) and discharge capacity are both ranked as Ti-NCM > Nb/Ti-NCM > Nb-NCM > NCM, which is consistent with the results of Li^+/Ni^{2+} mixing degree. Fig. 4b demonstrates the long cycling stabilities for samples. The capacity retention of Nb/Ti-NCM outstanding maintained 92.7% after 300 cycles at 1 C, much higher than 77.6% of the pristine sample. The discharge capacity for NCM has rapidly decayed to 136.5 mAh/g, as well as the capacity of Nb/Ti-NCM is kept 162.9 mAh/g. Interestingly, the enhanced capacity retention of Nb-NCM surpassed that of Ti-NCM, which may be attributed to the higher dissociation energy exhibited Nb–O bond (753 kJ/mol) in comparison to that of Ti–O bond (662 kJ/mol), enabling more effectively resist the evolution of lattice oxygen [45-47]. To further explore the origin of the rising capacity retention, the d*Q*/d*V* profiles of different cycles for samples are plotted in Fig. 4c and Fig. S8 (Supporting information). All samples experience a comparable process of phase transition (H1-M-H2-H3). The reversibility of phase transition, especially H2-H3, is associated positively with the cycle stability, the undesired reversibility exacerbating lattice stress to generate microcracks. Notably, the material polarization is reflected by the voltage offset (ΔV) of H2-H3 peaks in cycling. The ΔV of Nb/Ti-NCM (0.0095 V) is the lowest, and that of NCM is the largest (0.0315 V) after 300 cycles (Fig. 4c), indicating that the protection of Nb/Ti co-doping strategy effectively prohibits material polarization and improves reversibility. It is observed that Ti-NCM exhibits a lower reversibility of H2-H3 phase transition compared to that of Nb-NCM, which aligns with the outcome of cycle stability (Figs. S8b and c). The rate performance of samples at 0.1–10 C is shown in Fig. 4d. Nb/Ti-NCM exhibits an improved discharge capacity (144.3 mAh/g) at 10 C, which surpasses 129.7 mAh/g of NCM, owing to a reduced value of Li^+/Ni^{2+} mixing and the expansion of lattice parameter *c*, which broaden the Li^+ diffusion and facilitate the ion migration kinetic [48]. The diffusion coefficient of Li^+ (D_{Li^+}) has been gained by the galvanostatic intermittent titration technique (GITT) test, revealing that the D_{Li^+} is higher for Nb/Ti-NCM compared to that of NCM (Fig. 4e and Fig. S9 in Supporting information). The cycling abilities under harsh conditions, including expanded voltage window (2.7–4.5 V) and higher temperature of 45 °C for Nb/Ti-NCM and NCM cathode, were tested to further prove the advantages of Nb/Ti co-doping. Fig. S10 (Supporting information) displays the initial charge/discharge profiles and rate performance at a voltage range of 2.7–4.5 V. Notably, the discharge capacity of Nb/Ti-NCM is always higher than NCM from 0.1 C to 10 C (Fig. S10b). In addition, the capacity retention and ΔV of Nb/Ti-NCM (87.2% and 0.0336 V) after 200 cycles is superior to that of NCM (75.2% and 0.1152 V), as illustrated in Fig. 4f and Fig. S11 (Supporting information). Meanwhile, the cycling performances of both samples were evaluated at an elevated temperature of 45 °C within 2.7–4.3 V. After 200 cycles, the capacity retention for NCM declined severely to 68.4%. In contrast, the capacity retention of Nb/Ti-NCM is still maintained 87.3% (Fig. 4g). In addition, DSC is conducted to rationally access the

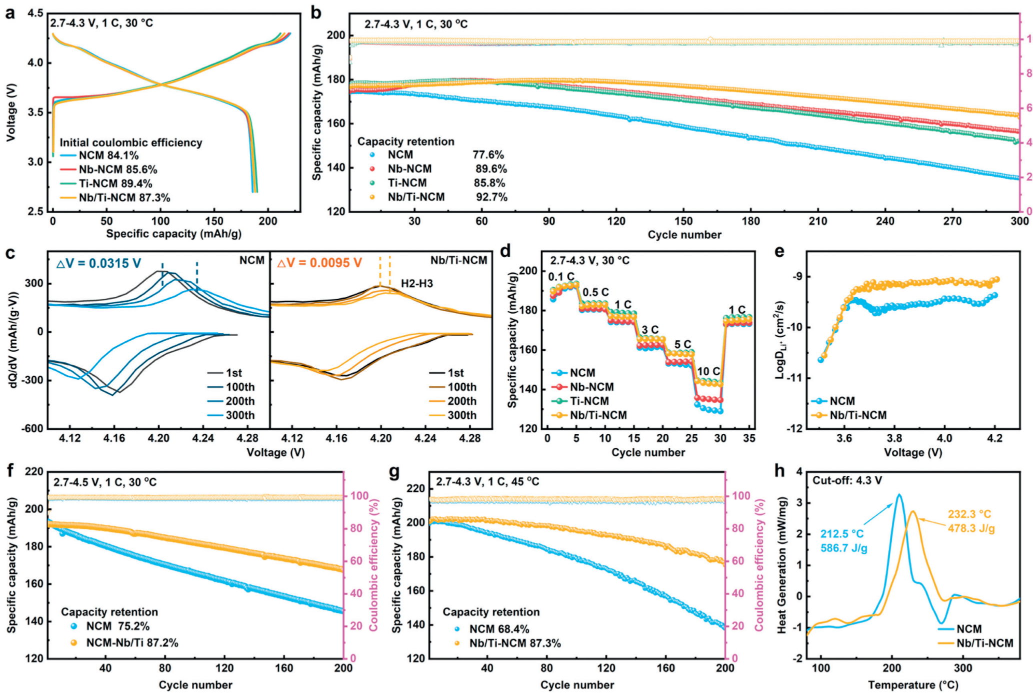

Fig. 4. Electrochemical performances of four cathodes within 2.7–4.3 V, 30 °C: (a) Initial charge-discharge curves, (b) cycle stabilities and (d) rate performances. (c) d*Q*/d*V* curves, (e) Li^+ diffusion coefficient of charging curves of NCM and Nb/Ti-NCM. (f) Cycle stabilities in the range of 2.7–4.5 V at 30 °C. (g) Cycle stabilities in the range of 2.7–4.3 V at 45 °C. (h) Differential scanning calorimeter (DSC) profiles of NCM and Nb/Ti-NCM after charging to 4.3 V.

thermal stability. The exothermic reaction peak of NCM cathode occurs at a lower temperature of 212.5 °C, compared to the Nb/Ti-NCM cathode which exhibits this peak at 232.3 °C. Moreover, the total heat release of Nb/Ti-NCM cathode is 478.3 J/g, which is considered minor compared to the 586.7 J/g of NCM cathode during the exothermic reaction. This demonstrates that Nb/Ti-NCM possesses better thermal stability. Comprehensive performance characterization shows that the Nb/Ti co-doping strategy effectively optimizes structural stability and Li-ion diffusion kinetics.

To further define the mechanism of Nb/Ti co-doping modification, *in-situ* XRD measurement has been utilized to elucidate the structural evolution during the initial charging and discharging process at 2.7–4.5 V. As displayed in Fig. 5, the lithiation/delithiation process involves a phase transition process of H1 → M → H2 → H3, which is accompanied with the angle shifts of the (003), (101), and (104) Bragg peaks. The NCM exhibits angular deviations of 0.955°, 0.959°, and 1.184° corresponding to (003), (101), and (104) crystal planes respectively, based on *in-situ* XRD data. Instead, the Nb/Ti-NCM displays lower offsets with 0.839°, 0.911°, and 1.107°. During the H1 → M → H2 phase transition, the (003) peak first skews toward a lower degree slowly, indicating that the *c*-axis expands slightly due to electrostatic repulsion within oxygen slabs broadening the space of Li slabs for the removal of Li^+. Subsequently, the lattice parameter *c* gradually decreases in the M-H2 phase transition stage due to the progressive oxidation of Ni, resulting in a shortened Ni–O bond length with a small lattice parameter contraction. Finally, the (003) peak undergoes a dramatic shift toward a higher angle in H2 → H3 phase transition process with *c*-axis sharp shrinkage. It is attributed to the remarkable reduction in electrostatic repulsion between the oxygen slabs caused by the shared negative charge of lattice oxygen transfer to higher valence nickel ion under a deeply delithiated state [49]. The (101) and (104) reflections appear a similar evolution that constantly shifts to a higher angle in charging, illustrating the *a*-axis continuous contraction [49-51]. The abrupt contraction of the lattice causes a concentration of anisotropic stress, which in turn triggers the development and spread of microcracks. Consequently, this process leads to a decline in particle integrity and eventual failure in performance. The variation of the cell parameters throughout the charging process was determined by calculation. As shown in Figs. 5c–e, the contraction variation ratio of the lattice parameter a (Δa), c (Δc), and cell volume (ΔV) for NCM are 2.67%, 4.14%, and 7.26%, respectively, whereas that for Nb/Ti-NCM are 2.35%, 3.12%, and 5.88%. These results show that the stronger Nb–O and Ti–O bond maintains electrostatic repulsion within oxygen slabs by alleviating the shared charge depletion lattice oxygen, thus mitigating the sharp contraction of the lattice parameters and enhancing the structural integrity of NCM cathode upon cycling.

To demonstrate the modification mechanism and surface reconstruction, post-mortem tests were operated on NCM and Nb/Ti-NCM electrodes after 200 cycles of 1 C. The cross-sectional morphologies of the two samples have been obtained by argon ion polishing and SEM. It is observed that none of the samples are fractured before cycling (Fig. S12 in Supporting information), however, after 200 cycles, the intergranular microcracks of the NCM secondary particles are numerous and tend to propagate toward the surface (Fig. 6a). In contrast, the Nb/Ti-NCM shows excellent mechanical integrity, implying that the Nb/Ti co-doping strategy effectively affirms the superior structure robustness, which is in favor of maintaining morphology complete and structural stability (Fig. 6b). As exhibited in Figs. 6c and d, the structural reconstructions of both samples have been visualized by HRTEM. The (111) and (104) crystal planes were investigated from the HRTEM image and corresponding FFT conversion of the NCM, which are matched with the rock salt phase of Ni–O (Fm-3m) and the layered (R-3m) structures, respectively, implying that a considerable degradation of the layered structure has been existed (within the white dashed line). Fortunately, the Nb/Ti-NCM simply shows the (006) crystal plane belongs to a layered structure preserved well intact.

However, the electrolyte not only reacts with the surface but also penetrates the interior along the cracks to aggravate the corrosion, resulting in a significant accumulation of rock salt phase

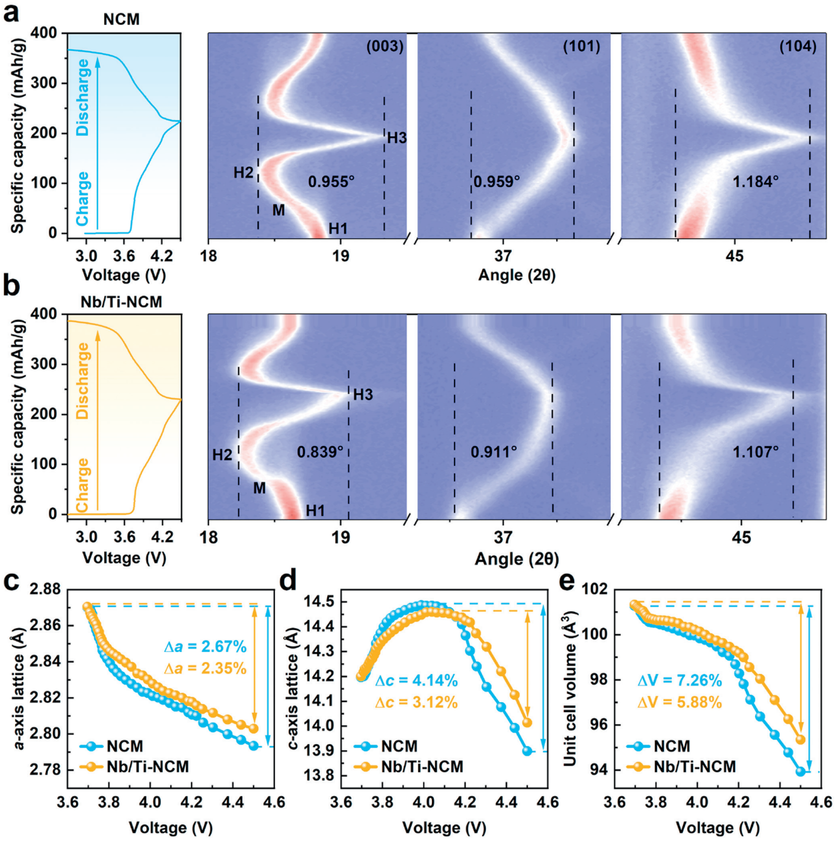

Fig. 5. *In situ* XRD patterns and the corresponding charge/discharge curves. (a) NCM and (b) Nb/Ti-NCM cathode. Lattice parameters variation of (c) *a*-axis, (d) *c*-axis, (e) cell volume of NCM and Nb/Ti-NCM cathode at the charge state.

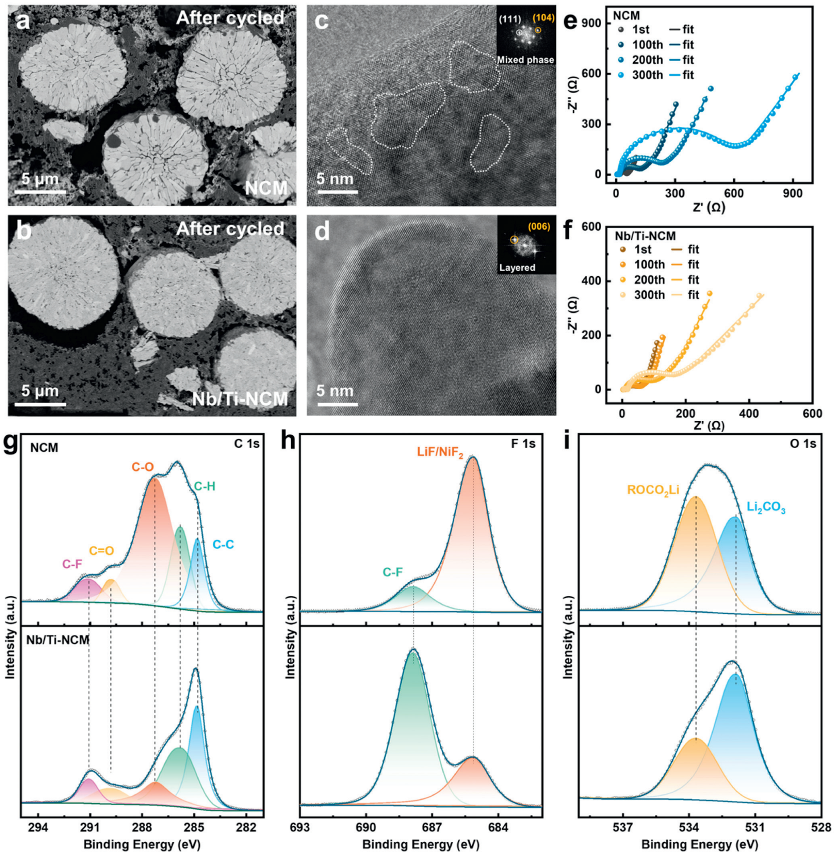

Fig. 6. Cross-sectional SEM images of (a) NCM and (b) Nb/Ti-NCM after 200 cycles at 1 C. High-resolution TEM images and FFT patterns of (c) NCM and (d) Nb/Ti-NCM. Nyquist plots of (e) NCM and (f) Nb/Ti-NCM at 2.7–4.3 V after every 100th cycle. (g) C 1s, (h) F 1s, (i) O 1s XPS spectra for NCM and Nb/Ti-NCM after 200 cycles at 1 C.

(Ni–O) that is electrochemically inactive, leading to Li-ion transport impeded, stress inhomogeneity exacerbated, and crack propagation aggravated [52]. To assess the impact of microcracks and side reactions on the deterioration of cathode structure, electrochemical impedance spectra (EIS) have been recorded every 100 cycles at the charge state to monitor the impedance changes. All curves are comprised of two semi-circles and a slope line. The resistance of the solution can be inferred from the point where the real axis is intercepted. The resistance for Li^+ across the surface-film of the cathode (R_{sf}) is associated with the initial semicircle observed at high frequency, and the charge-transfer resistance (R_{ct}) is defined by the following semicircle in the mid-frequency region. The subsequent slope line in the low-frequency region represents the Warburg impedance (Z_w), indicating the diffusion of Li-ions [53,54]. The experiment data and fitting result are shown in Figs. 6e and f and Table S7 (Supporting information). The equivalent circuit is provided in Fig. S13 (Supporting information). The R_{ct} value of NCM and Nb/Ti-NCM are 27.6 Ω and 23.9 Ω after activation of 2 cycles at 0.1 C. However, after 300 cycles, the R_{ct} of the former rapidly increases to 555.4 Ω, while that of the latter is just 116.5 Ω. The dramatic increment of R_{ct} indicates that side reactions and cracks in the NCM severely impede charge transfer, giving rise to structural collapse and deterioration of cycling stability, which is further proven by the calculation of D_{Li^+} (Fig. S14 in Supporting information). Moreover, the surface chemical compositions of NCM and Nb/Ti-NCM after cycling were characterized by XPS. As illustrated in Figs. 6g–i, it is evident that NCM cathode demonstrates higher intensities for the C–O, $ROCO_2Li$, and LiF/NiF_2 species compared to those of Nb/Ti-NCM, which means a more pronounced decomposition of polyvinylidene and deterioration of $LiPF_6$ side reaction more severe [55].

In summary, the dopant formation energy of Nb or Ti was calculated by DFT in this study, and a straightforward solid-phase method for synthesizing Nb/Ti co-doping NCM cathode materials was proposed. The co-doping sample exhibits superior electrochemical performance, with a discharge capacity of 144.3 mAh/g at the current density of 10 C, surpassing that of NCM (129.7 mAh/g). Furthermore, the capacity retention maintains optimistically 92.7% after 300 cycles at 1 C (30 °C). Even at an elevated temperature of 45 °C, capacity retention remains 87.3% after 200 cycles within 2.7–4.3 V. These improvements can be ascribed to the boosted structural stability for stronger Nb–O and Ti–O binding energies, which effectively inhibit the depletion of negative charge from oxygen and protect against lattice distortion during H2-H3 phase transition. The Ti element introduced can powerfully restrain Li^+/Ni^{2+} mixing. The synergetic effect of Nb and Ti remarkably mitigates the formation of microcracks and reduces detrimental interaction between layered cathode and organic electrolyte. This study promotes a novel approach for the development of Ni-rich layered cathode materials with high performance.

Declaration of competing interest

The authors declare that they have no known competing financial interests or personal relationships that could have appeared to influence the work reported in this paper.

CRediT authorship contribution statement

Mingzhu Jiang: Writing – review & editing, Writing – original draft, Visualization, Methodology, Investigation, Data curation, Conceptualization. **Panqing Wang:** Investigation. **Qiheng Chen:** Data curation. **Yue Zhang:** Project administration. **Qi Wu:** Validation. **Lei Tan:** Methodology. **Tianxiang Ning:** Supervision. **Lingjun Li:** Writing – review & editing, Supervision, Funding acquisition, Data curation. **Kangyu Zou:** Writing – review & editing, Conceptualization.

Acknowledgment

This work was financially supported by the National Natural Science Foundation of China (Nos. 52374299, 52304320 and 52204306), Outstanding Youth Foundation of Hunan Province (No. 2023JJ10044), Key Project of Hunan Provincial Department of Education (No. 22A0211), and Natural Science Foundation of Hunan Province (No. 2023JJ40014).

Supplementary materials

Supplementary material associated with this article can be found, in the online version, at doi:10.1016/j.cclet.2024.110040.

References

[1] H. Li, L. Wang, Y. Song, et al., Adv. Mater. 36 (2024) 2312292.
[2] H. Yu, Y. Cao, L. Chen, et al., Nat. Commun. 12 (2021) 4564.
[3] M. Zhou, J. Zhao, X. Wang, et al., Chin. Chem. Lett. 34 (2023) 107793.
[4] Q. Gan, N. Qin, H. Yuan, et al., Energy Chem. 5 (2023) 100103.
[5] W. Zheng, Q. Liu, Z. Wang, et al., Energy Storage Mater. 28 (2020) 300–306.
[6] Y.K. Sun, Z.H. Chen, H.J. Noh, et al., Nat. Mater. 11 (2012) 942–947.
[7] C.H. Jung, D.H. Kim, D. Eum, et al., Adv. Funct. Mater. 31 (2021) 2010095.
[8] X.Q. Zeng, C. Zhan, J. Lu, K. Amine, Chem. 4 (2018) 690–704.
[9] C. Wang, L. Tan, H.L. Yi, et al., Nano Res. 15 (2022) 9038–9046.
[10] Z.X. Guo, G.D. Qian, C.Y. Wang, et al., Prog. Nat. Sci. Mater. Int. 33 (2023) 1–7.
[11] C. Liang, L.H. Jiang, Z.S. Wei, et al., J. Energy Chem. 65 (2022) 424–432.
[12] L. Zhang, D. Liu, J. Huang, et al., J. Energy Storage 78 (2024) 110073.
[13] S. Niu, J. Xu, K. Wu, et al., Mater. Chem. Phys. 260 (2021) 124046.
[14] J. Lu, C. Zhan, T. Wu, et al., Nat. Commun. 5 (2014) 5693.
[15] M.Y. Ge, S.G. Wi, X. Liu, et al., Angew. Chem. Int. Ed. 60 (2021) 17350–17355.
[16] W. Huang, W. Li, L. Wang, et al., Small 17 (2021) 2104282.
[17] L.J. Li, L.Z. Fu, M. Li, et al., J. Energy Chem. 71 (2022) 588–594.
[18] Z. Jiang, S. Chen, C. Wei, et al., Chin. Chem. Lett. 35 (2024) 108561.
[19] M. Lu, Z. Wang, G. Luo, et al., Chin. Chem. Lett. 35 (2024) 108638.
[20] R. Wang, X. Dai, Z. Qian, et al., ACS Mater. Lett. 2 (2020) 280–290.
[21] Q. Gan, N. Qin, H. Guo, et al., ACS Energy Lett. 9 (2024) 1562–1571.
[22] X. Fan, X. Ou, W. Zhao, et al., Nat. Commun. 12 (2021) 5320.
[23] Y.H. Du, H. Sheng, X.H. Meng, et al., Nano Energy 94 (2022) 106901.
[24] Y. Sun, W. Huang, G. Zhao, et al., ACS Energy Lett. 8 (2023) 1629–1638.
[25] X. Wang, B. Zhang, Z. Xiao, et al., Chin. Chem. Lett. 34 (2023) 107772.
[26] H. Wu, X. Zhou, C. Yang, et al., ACS Appl. Mater. Interfaces 15 (2023) 18828–18835.
[27] W. Yang, H. Li, D. Wang, et al., Nano Energy 104 (2022) 107880.
[28] K. Zhang, Y. Tian, X. Chen, S. Hu, Z. Jian, Chin. Chem. Lett. 35 (2024) 108308.
[29] Y. Ming, W. Xiang, L. Qiu, et al., ACS Appl. Mater. Interfaces 12 (2020) 8146–8156.
[30] M. Yi, A. Dolocan, A. Manthiram, Adv. Funct. Mater. 33 (2023) 2213164.
[31] H. Zhu, Z. Wang, L. Chen, et al., Adv. Mater. 35 (2023) 2209357.
[32] Y.J. Sun, C.H. Wang, W.J. Huang, et al., Angew. Chem. Int. Ed. 62 (2023) e202300962.
[33] H. Yang, H.H. Wu, M. Ge, et al., Adv. Funct. Mater. 29 (2019) 1808825.
[34] Y.F. Xie, F.Y. Guo, Y.X. Zhang, J. Alloys Compd. 981 (2024) 173592.
[35] X.X. Tan, W.J. Peng, M. Wang, et al., Prog. Nat. Sci. Mater. Int. 33 (2023) 108–115.
[36] J.Q. Peng, Y.Y. Wei, D.M. Liu, et al., Rare Met. 43 (2024) 658–670.
[37] X. Li, T. Lai, A. Sheng, et al., J. Energy Storage 72 (2023) 108262.
[38] Z. Wang, H. Zhu, H. Yu, et al., Chin. Chem. Lett. 34 (2023) 107718.
[39] X. Huang, J.Q. Zhao, W.C. Zhu, et al., J. Energy Chem. 63 (2021) 376–384.
[40] M.K. Shobana, J. Alloys Compd. 802 (2019) 477–487.
[41] J. Yang, Y. Li, X. Xi, et al., Energy Environ. Mater. 6 (2022) e12574.
[42] X.A. Zhou, F.L. Zhang, X.L. Fu, et al., Energy Storage Mater. 52 (2022) 19–28.
[43] J.P. Wang, X.B. Lu, Y.C. Zhang, et al., J. Energy Chem. 65 (2022) 681–687.
[44] H. Wang, Y. Chu, Q. Pan, et al., ACS Sustain. Chem. Eng. 9 (2021) 8951–8961.
[45] D.Y. Hwang, S.J. Sim, B.S. Jin, H.S. Kim, S.H. Lee, ACS Appl. Energy Mater. 4 (2021) 1743–1751.
[46] H.H. He, J. Dong, D.Y. Zhang, C.K. Chang, Ceram. Int. 46 (2020) 24564–24574.
[47] J.L. Wang, Z.C. Yi, C.J. Liu, et al., J. Colloid Interface Sci. 635 (2023) 295–304.
[48] F.K. Li, Z.B. Liu, J.D. Shen, et al., J. Mater. Chem. A 9 (2021) 2830–2839.
[49] H. Yu, H. Zhu, H. Jiang, et al., Natl. Sci. Rev. 10 (2023) nwac166.
[50] L. Ni, H. Chen, S. Guo, et al., Adv. Funct. Mater. 33 (2023) 2307126.
[51] Y.Y. Huang, Y.C. Zhu, H.Y. Fu, et al., Angew. Chem. Int. Ed. 60 (2021) 4682–4688.
[52] H. Li, P.F. Zhou, F.M. Liu, et al., Chem. Sci. 10 (2019) 1374–1379.
[53] J. Shen, B. Zhang, A. Dai, et al., J. Power Sources 559 (2023) 232653.
[54] J.S. Lee, Y.J. Park, ACS Appl. Mater. Interfaces 13 (2021) 38333–38345.
[55] K. Zou, S. Xie, M. Jiang, et al., Chem. Eng. J. 483 (2024) 149189.